Irradiation-induced amorphization of $Cd_2Nb_2O_7$ pyrochlore

A. Meldrum
Department of Physics, University of Alberta, Edmonton, Alberta, Canada T6G 2J1

C. W. White, V. Keppens,* and L. A. Boatner
Solid State Division, Oak Ridge National Laboratory, Oak Ridge, Tennessee 37831

R. C. Ewing
Department of Nuclear Engineering and Radiological Sciences, University of Michigan, Ann Arbor, Michigan 48109-2104
(Received 25 August 2000; published 20 February 2001)

Several investigations have recently been undertaken in order to achieve a more complete understanding of the radiation-damage mechanisms in $A_2B_2O_7$ pyrochlore-structure compounds. The present work represents the first systematic study of the irradiation-induced amorphization of a pyrochlore with *A*- and *B*-site cation valences of +2 and +5, respectively. Relatively large single crystals of $Cd_2Nb_2O_7$ were grown for these experiments. *In situ* ion-irradiation experiments were carried out in a transmission electron microscope in conjunction with *ex situ* Rutherford backscattering measurements of ion-irradiated $Cd_2Nb_2O_7$ single crystals. $Cd_2Nb_2O_7$ can be amorphized *in situ* by Ne or Xe ions at temperatures up to 480 and 620 K, respectively. At room temperature, the amorphization fluence was 36 times higher for 280 keV Ne^+ than for 1200 keV Xe^{2+}, corresponding to a displacement dose that was higher by a factor of 3. Disordering of Cd and Nb over the available cation sites occurs at intermediate ion doses prior to amorphization. The temperature dependence of the amorphization dose is modeled, and the results are compared to those of a previous model. The bulk-sample Rutherford backscattering spectroscopy (RBS) results were generally consistent with the *in situ* TEM measurements. Effects of crystallographic orientation and ion charge state had relatively little effect on the damage accumulation in bulk crystals. The RBS data are consistent with a defect-accumulation, cascade-overlap model of amorphization of $Cd_2Nb_2O_7$, as are the *in situ* TEM observations.

DOI: 10.1103/PhysRevB.63.104109 PACS number(s): 61.80.Jh, 61.43.Er, 61.82.Ms, 28.41.Kw

INTRODUCTION

The study of radiation effects in complex oxides is currently an active field of research due, in part, to the potential use of these materials as nuclear waste forms for the storage or disposal of actinide elements. The oxide phases that occur in a specific polyphase ceramic nuclear waste form first developed in Australia and known as Synroc[1] are of particular interest because some of these phases (pyrochlore and zirconolite) are currently being considered for use in the immobilization of plutonium resulting from the dismantling of nuclear weapons.[2,3] Synroc nominally consists of three main actinide-bearing phases: zirconolite (ideally $CaZrTi_2O_7$), pyrochlore ($^{VIII}A_2^{VI}B_2O_7$), and perovskite ($CaTiO_3$).

The present investigation focuses on the study of radiation-damage effects in pyrochlore—a phase whose main structural units were first determined by von Gaertner in 1930.[4] Structurally, pyrochlore consists of interconnected AO_8 and BO_6 cation polyhedra[5] where the BO_6 octahedra are slightly distorted and form a continuous corner-sharing network (Fig. 1). The large, eight-fold coordinated *A*-site cations and the seventh oxygen occupy channels in the $(B_2O_6)_\infty$ network of octahedra.[5,6] The structure is an anion-deficient MX_2 fluorite structure in which the *A* and *B* cations are ordered on the *M* sites. One-eighth of the *X* anions are absent in the pyrochlore structure, and the resulting oxygen vacancies are ordered on the anion sublattice.[6] The crystal structure of pyrochlore can accommodate a variety of cations, including the actinides[7] on the *A* site. In most pyrochlores, the *A*- and *B*-site cations have valences of either +3 and +4 or +2 and +5, respectively. The Synroc nuclear-waste ceramics currently of interest contain $Gd_2Ti_2O_7$ as a major constituent phase[1,8] where the actinides preferentially partition onto the large *A*-cation site and can substitute for Gd in relatively large proportions (in fact, pure $Pu_2Ti_2O_7$ has been

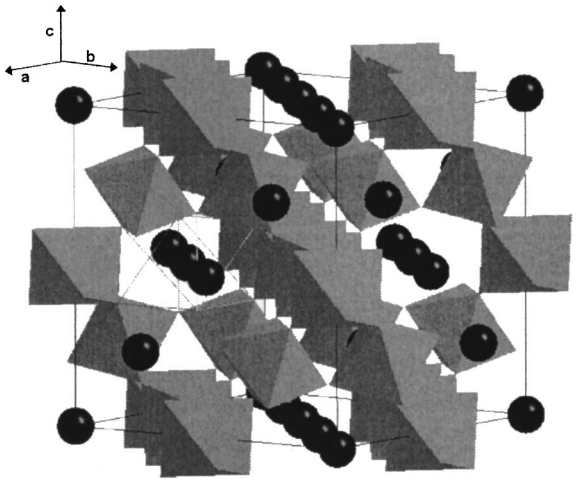

FIG. 1. Crystal structure of pyrochlore. The *B*-site cations are located at the centers of the shaded octahedra. The large *A*-site cations (black spheres) occupy channels in the corner-sharing network of BO_6 octahedra.

produced).[9] The zirconate phases $Gd_2Zr_2O_7$ (Ref. 10) and $Pu_2Zr_2O_7$ (Refs. 11 and 12) have recently been synthesized and are also being investigated as candidate phases for the immobilization of weapons-grade Pu.

Due to the occurrence of actinide-bearing pyrochlore in Synroc and other titanate-based nuclear waste forms, several previous studies have been undertaken to investigate the effects of radiation damage in these Ti-rich compositions. Specifically, an early study[13] showed that ^{244}Cm-doped synthetic $Gd_2Ti_2O_7$ became predominantly amorphous after a dose of 2.3×10^{25} alpha decays/m^3—demonstrating that this phase is highly susceptible to irradiation-induced amorphization at room temperature. In a detailed investigation of U- and Th-bearing natural Ti-pyrochlore,[14] the saturation dose for amorphization was found to increase with the age of the specimens—an observation implying that gradual, long-term recrystallization of these phases occurs in the geologic environment. More recently, ion-beam techniques combined with *in situ* transmission electron microscopy have been used to obtain the temperature dependence of the amorphization dose in pyrochlore containing a variety of *A*-site cations, including mixtures of Ca, U,[15,16] and various lanthanides.[17] These compounds are easily amorphized at room temperature, and in fact, amorphization can be induced at temperatures as high as 1030 K. The substitution of Zr for Ti on the *B* site dramatically increases the ''resistance'' to amorphization to the point where ion-beam-induced amorphization does not occur at room temperature in $Gd_2Zr_2O_7$.[10]

The previous studies of radiation-damage effects in pyrochlores have employed either impure natural crystals with relatively uncertain geological histories or polycrystalline synthetic, pressed, and sintered pellets. All previous ion-beam investigations have used pyrochlores of the +3,+4 cation valence group. In the present work, we investigate the effects of ion irradiation using relatively large (up to 15 $\times15\times5$ mm) high-purity synthetic single crystals of the cadmium/niobium +2,+5 pyrochlore, $Cd_2Nb_2O_7$. Large single crystals of this phase can be readily grown, thereby providing a unique opportunity to combine both single-crystal ion implantation and Rutherford backscattering spectroscopy (RBS) analysis experiments with transmission electron microscopy (TEM) studies of the effects of *in situ* ion irradiation. The combination of these techniques provides important new information regarding the mechanisms responsible for ion-irradiation-induced amorphization in the $Cd_2Nb_2O_7$ phase.

EXPERIMENT

Crystal growth

Single crystals of $Cd_2Nb_2O_7$ were grown by means of a high-temperature solvent (flux) technique. The growth process was carried out using 50-mL Pt crucibles that were placed in a temperature-programmable furnace employing SiC heating elements. A crystal-growth charge consisting of a stoichiometric mixture of CdO and Nb_2O_5 was added to a cadmium borate flux produced by the reaction of additional CdO and B_2O_3. This growth charge was heated to 1250 °C over a 5-h period and held at that temperature for 3 h. The furnace was then slowly cooled from 1250 to 1050 °C over a 240-h period. The furnace was then turned off and allowed to cool to room temperature, at which point the resulting $Cd_2Nb_2O_7$ single crystals were mechanically removed from the remaining solidified flux. Any additional adhering flux was removed using a solution of HCl. The crystals ranged in size from ~2 mm to upward of 15 mm and are, therefore, some of the largest synthetic single crystals of pyrochlore reported to date. The $Cd_2Nb_2O_7$ pyrochlore phase was confirmed by x-ray powder-diffraction analysis.

TEM *in situ* ion irradiation

Crystals of $Cd_2Nb_2O_7$ grown as described above were prepared for the *in situ* ion-irradiation/TEM analysis experiments by hand polishing to a thickness of approximately 10 μm and subsequent ion milling to perforation at room temperature using 4-keV Ar^+ ions at an incident angle of 20°. These specimens were then irradiated *in situ* in an electron microscope at the HVEM-Tandem Facility at Argonne National Laboratory. This facility consists of a tandem ion accelerator interfaced to a modified Kratos/AEI transmission electron microscope,[18] allowing ion irradiation to be performed *during* TEM observation. The irradiations were carried out with either 1200-keV Xe^{2+} or 280-keV Ne^+ ions at temperatures from 20 to 1100 K. These relatively high ion energies were chosen so that most of the ions pass completely through the electron transparent part of the specimen. The ion flux was 1.7×10^{12} $cm^{-2}s^{-1}$. The electron microscope was operated at 300 kV, and the electron beam was not incident on the specimen for most of the ion-irradiation time. Selected-area electron diffraction was used to determine the dose necessary to amorphize the specimen. The experiments were continued until the electron-diffraction maxima disappeared, as determined by visual examination of the phosphor screen, and the electron-diffraction pattern consisted only of the diffuse halo characteristic of an amorphous material. The thickness of the specimens was estimated to be ~100 nm by using combined thickness-fringe and convergent-beam electron-diffraction measurements. The room-temperature experiments were repeated three times in order to estimate the mean deviation. This was converted to a percentage of the average value, and the same percentage was used to calculate error bars on all the data points.

Rutherford backscattering analysis

The larger $Cd_2Nb_2O_7$ crystals that also exhibited high-quality growth faces were selected for use in the combined ion implantation and RBS analysis experiments. The most highly developed growth faces corresponded to the {111} family of crystallographic planes, and these were used for most of the experiments. Because of the high quality of the {111} growth faces of the single-crystal specimens, no mechanical polishing or annealing treatments were required. Some of the largest crystals were sectioned with a wire saw perpendicular to the [100] direction so that the orientational dependence of the damage accumulation could be deter-

mined. The surfaces of these (100)-plane wafers were polished to a 0.05-μm finish using suspensions of diamond and colloidal silica.

The specimens were mounted by spring clipping onto a steel backing plate for ion implantation. One-half of each sample was masked and was not implanted. The beam current was less than 0.5 μA/cm^2 so thermally conductive paint was not applied. The duration of the implant was from seconds to a few minutes. All of the implantations were carried out at room temperature. The samples were tilted 7° away from the incident ion beam to minimize channeling effects. Specimens were irradiated with either 320-keV Xe^{2+} to fluences ranging from 5×10^{12} to 1×10^{15} ions/cm^2, or with 70-keV Ne^+ to fluences from 3×10^{14} to 1×10^{16} ions/cm^2. At these energies, both ion types have a projected range of approximately 60 nm. The specimens were implanted to a low-ion fluence and were then removed from the implanter, and RBS in the channeling mode was performed using a 2.3-MeV He^+ ion beam with the detector at an angle of 160° relative to the incident He^+ beam. Each specimen was initially aligned in the usual manner by finding the minimum yield in the unimplanted (masked) portion of the crystal. The specimen was then linearly translated so that the He beam impinged on the implanted region of the crystal, and a new spectrum was obtained. Random yields were obtained by tilting the unirradiated part of the crystal away from the zone axis and then rotating over an angle of ±5° during data collection. The specimens were subsequently returned to the ion implanter for the accumulation of an additional ion dose, and the process was repeated until the channeling yield from the near-surface region matched the random yield.

RESULTS AND DISCUSSION

Ion irradiation *in situ* in the TEM

$Cd_2Nb_2O_7$ was amorphized at room temperature by both the Ne^+ and Xe^{2+} irradiations in a two-step crystalline-to-amorphous transformation process. At low fluences (i.e., less than one-third of the total fluence for amorphization), the {022} diffraction maxima from the pyrochlore lattice gradually disappeared, but the {044} maxima remained intense (see Fig. 2). The unit-cell volume was, therefore, reduced by a factor of 8 as a result of disordering of the *A*- and *B*-site cations and the anion vacancies. With increasing dose, the {044} diffraction spots gradually decreased in intensity, and, concurrently, a diffraction halo characteristic of an amorphous phase increased in intensity. This type of disordering prior to amorphization has been documented previously for other compositions of pyrochlore.[15–17] The electron-diffraction patterns presented in Fig. 2 for the case of Ne^+ irradiation show that, in fact, $Cd_2Nb_2O_7$ does not become amorphous directly, but rather that it transforms to the disordered defect-fluorite structure at intermediate ion doses. For the Xe^{2+} irradiation, a similar evolution is observed by electron diffraction.

In order to make comparisons of radiation-damage effects due to different incident ions, the fluence for amorphization was converted to dose in units of displacements per atom

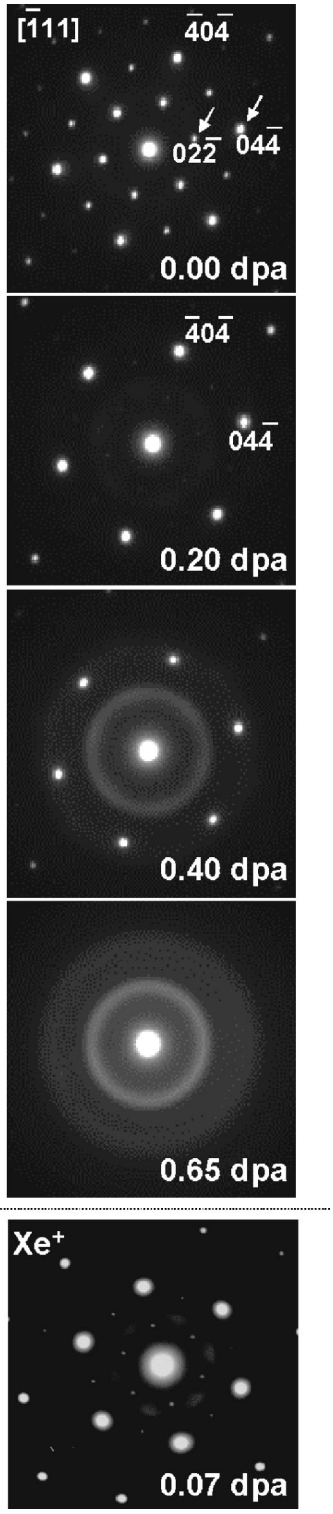

FIG. 2. A sequence of electron-diffraction patterns for a [111] zone axis of $Cd_2Nb_2O_7$ irradiated with an increasing dose of 280-keV Ne ions is shown and compared with the diffraction pattern for an unirradiated specimen illustrated in the top image. The dose in displacements per atom is shown in the lower-right-hand corner of each diffraction pattern. The lowermost diffraction pattern is for Xe-ion-irradiated $Cd_2Nb_2O_7$ corresponding to an ion dose of 0.07 dpa (i.e., comparible to 0.20 dpa for Ne irradiation).

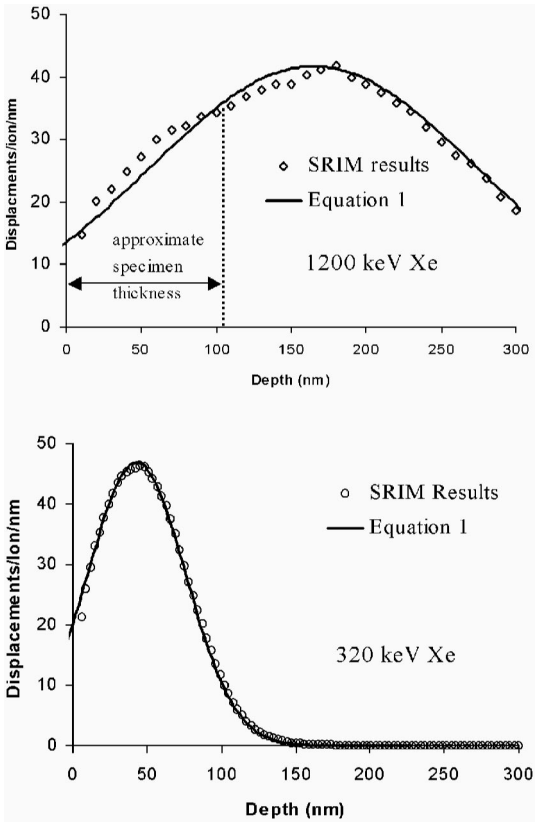

FIG. 3. The number of displacements per ion for 1200-keV Xe (top) or 320-keV Xe (bottom) in $Cd_2Nb_2O_7$, calculated using the Monte Carlo code SRIM (circles). The solid line represents the solution to Eq. (1). Equation (1) fits the SRIM results quite well, especially for the lower ion energy. Similar results were obtained for Ne ions in $Cd_2Nb_2O_7$. Equation (1) was, therefore, used to obtain the value of N used in the fluence-to-dose conversions.

(dpa). This conversion requires some knowledge of the average number of displacements per ion (N) throughout the thickness of the specimen. This, in turn, requires the atomic displacement energies, which have not been determined for any pyrochlore composition. In order to be consistent with previous investigations,[16,17] we have assumed an E_d of 25 eV. Accordingly, by assuming a displacement energy of $\sim$25 eV, the average number of displacements per ion can be estimated as a function of depth for $Cd_2Nb_2O_7$ using the Monte Carlo code SRIM[19] in the ''full cascade'' mode. In previous work on pyrochlore-structure phases[17] the number of displacements per ion at the exit surface of the sample represented the point used to estimate N. This will result in a slight overestimate of the actual displacement dose because the nuclear stopping power increases as the ions traverse the thickness of the specimen. Alternatively, one could use the value calculated at one-half of the total specimen thickness. Another technique is to model the SRIM results by using the following simple Gaussian distribution:

$$d = \frac{Z}{\sigma^2\sqrt{2\pi}} \exp\left[\frac{-(x-R)^2}{2\sigma^2}\right], \qquad (1)$$

TABLE I. Ion fluence for amorphization of $Cd_2Nb_2O_7$ pyrochlore.

Ion	Temperature (K)	Fluence $\times 10^{14}$ ions/cm^2
Ne^+ (280 keV)	20	11.1
	100	11.4
	130	12.9
	303	25.5
	403	36.6
Xe^{2+} (1200 keV)	20	0.3
	130	0.3
	303	0.7
	473	0.9
	573	2.0
	623	17.0
	673	44.2

where d is the number of displacements per ion at a depth x, R is the ion range, σ is the straggling (or standard deviation), and Z is a constant. Both Z and σ are parameters that are fit to match the SRIM calculations. Here, the fit is quite good, as shown in Fig. 3. The appropriate number of displacements throughout the specimen thickness was then calculated by integrating Eq. (1) from $x=0$ to $x=100$ nm (the estimated thickness of the specimen), and the average was obtained by dividing the result by the specimen thickness. The displacement dose (D) was then obtained by the simple conversion $D=N\phi/A$, where N is obtained from fitting Eq. (1) to the SRIM results, ϕ is the measured amorphization fluence, and A is the atomic density of $Cd_2Nb_2O_7$ (7.86×10^{22} cm^{-3}).

The ion fluence required for the amorphization of $Cd_2Nb_2O_7$, as measured by electron diffraction, is given in Table I. These values were converted to an amorphization dose (D_c) in dpa as described above. The temperature dependence of the amorphization dose for the Ne^+ and Xe^{2+} ion irradiation of $Cd_2Nb_2O_7$ is plotted in Fig. 4. For Ne^+ irradiation, the amorphization dose is relatively constant at $\sim$0.3 dpa at temperatures below $\sim$150 K. At approximately room temperature, the amorphization dose begins to increase more rapidly, and the critical temperature (T_c), i.e., the temperature above which amorphization cannot be induced, is above 400 K. The same basic features occur for Xe^{2+} irradiation of $Cd_2Nb_2O_7$, except that the amorphization dose at low temperatures is three times lower than that for the irradiation with Ne^+. For the Xe^{2+} irradiation, the amorphization dose does not increase significantly until temperatures above 500 K are reached, and in this case, T_c is slightly above 600 K.

Several models have been developed that relate the amorphization dose to temperature and thereby define the critical temperature and activation energy for recrystallization.[20–23] There is considerable debate in the literature over which model is most appropriate for ion irradiation of complex ceramics.[24,25] In Fig. 4, we plot one of the simplest models to

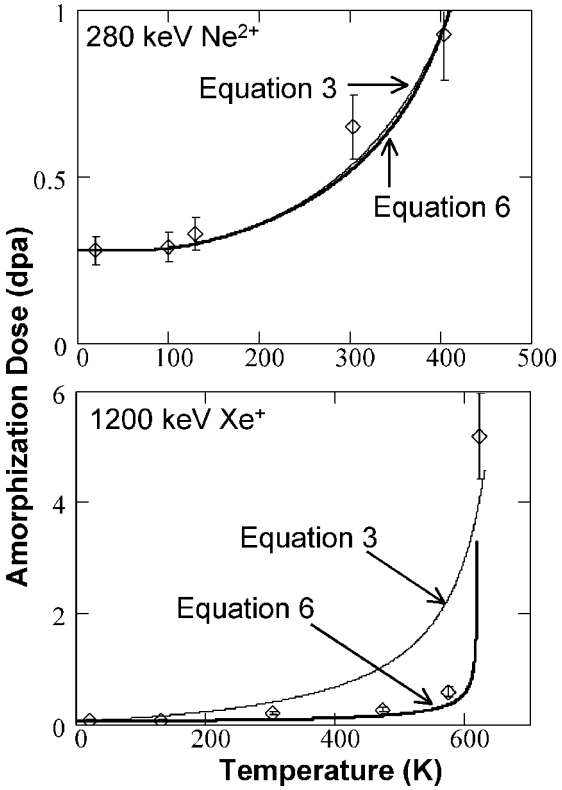

FIG. 4. Temperature dependence of the amorphization dose for irradiation of $Cd_2Nb_2O_7$ with 280-keV Ne^+ (top) or 1200-keV Xe^{2+} (bottom) as determined from *in situ* irradiations in the TEM. The thin curves are calculated on the basis of a least-squares regression to Eq. (3) and the solid curves are obtained from Eq. (6).

the experimental data. According to this model, the temperature dependence of the amorphization dose is given by[26]

$$\frac{df_a}{dt}=[\phi\sigma_a-\tau^{-1}\exp(-E_a/kT)](1-f_a). \tag{2}$$

Here, f_a is the amorphous fraction, t is time, ϕ is the ion fluence, σ_a is the amorphization cross section, τ is a time constant, and E_a is an activation energy for recrystallization. The damage production term is given by $\phi\sigma_a$. Weber *et al.*[26] replace f_a and σ_a with f_d and σ_d to model a damaged, as opposed to an amorphous, fraction. This equation has often been used to model the temperature dependence of the amorphization dose for complex ceramics [e.g., Refs. 24–29]. In Eq. (2), a recrystallization term is subtracted directly from the damage production term, and $1-f_a$ is the probability for an incoming ion to strike remaining undamaged material. When the damage term is set to zero, Eq. (2) predicts a maximum recrystallization rate at $f_a=0$. This implies that Eq. (2) may not be a useful approximation if there is post-cascade recrystallization. The solution to Eq. (2) under the constraints that $f_a=0$ at $t=0$ is given by[26]

$$\ln\left(1-\frac{D_0}{D_c}\right)=\ln\left(\frac{1}{\phi\sigma_a\tau}\right)-\frac{E_a}{kT}, \tag{3}$$

where D_0 is the amorphization dose at 0 K (determined by extrapolation in Fig. 4), and D_c is the amorphization dose above 0 K. The critical temperature can be obtained by setting D_c equal to infinity and solving for T_c:

$$T_c=\frac{E_a}{k\ln(1/\phi\sigma_a\tau)}. \tag{4}$$

Equation (3) was fit to the experimental data by allowing E_a and $\ln(1/\phi\sigma_a\tau)$ to vary until the least-squares difference between the calculated and measured amorphization dose at each temperature was minimized. The model fits the Ne^+ irradiation data quite well. Equation (4) predicts a critical temperature of 580 K for the Ne^+ irradiation of $Cd_2Nb_2O_7$. For the case of the Xe^{2+} irradiation, however, Eq. (3) gives a more gradual increase in D_c with temperature than is observed experimentally (Fig. 4).

For comparison, the recrystallization of amorphous material can be directly modeled with the following differential equation:

$$\frac{df_a}{dt}=P(1-f_a)-\lambda_a f_a(1-f_a). \tag{5}$$

Here, P is the dose rate (in dpa/s) and λ_a is a recrystallization term [$\lambda_a=\tau^{-1}\exp(-E_a/kT)$, where τ is a time constant]. Similar to Eq. (2), the damage accumulation is proportional to $1-f_a$. The damage rate is largest in the fully crystalline material and approaches zero at $f_a=1$. Equation (5) assumes that recrystallization is most rapid for $f_a=0.5$ (i.e., when there is the maximum amount of crystalline-amorphous interface). A recrystallization probability of this type was recently suggested to be appropriate for ion-irradiated ceramics.[24] The solution to Eq. (5), under the constraint that $f_a=0$ at $t=0$ is

$$D_c=\frac{\left[\ln P-\ln\left(\frac{P-\lambda_a f_a}{1-f_a}\right)\right]}{\left(\frac{\lambda_a}{P}-1\right)C}, \tag{6}$$

where C is a scaling parameter that relates the damage production rate P to the Kinchin-Pease displacement rate: $C=-\ln(1-f_a)/D_0$.[25] To calculate the curve in Fig. 4, we assumed an amorphous fraction of 0.95 and P is 0.002 dpa/s. Previous work demonstrated that a specimen appears completely amorphous by electron diffraction at $f_a=0.95$.[30] In Eq. (5), the critical temperature can be determined by setting the damage rate P equal to the recrystallization rate λ_α.[24,25] Solving for the temperature gives

$$T_c=\frac{-E_a}{k\ln\left(\frac{P}{\tau}\right)}. \tag{7}$$

Equation (6) gives a good fit to the experimental data (Fig. 4). For high values of τ and E_a, the curvature of the fitted line is quite steep, whereas, for low values the temperature rate of increase in dose is less sharp. Equation (6)

TABLE II. Comparison of activation energies and critical temperatures obtained by solving Eqs. (3) and (6). The amorphization dose at 0 K (extrapolated) and at room temperature is given in the final two columns.

ion	E_a (eV)		T_c (K)		D_0 (0 K)	D_c (RT)
	Eq. (3)	Eq. (6)	Eq. (3)	Eq. (6)	dpa	dpa
Ne^+	0.04	0.04	580	480	0.28	0.65
Xe^{2+}	0.01	0.08	695	620	0.09	0.22

closely matches both the Ne^+ and the Xe^{2+} irradiation results. The activation energies obtained for the recrystallization are extremely low [a few hundredths of an eV, similar to Eq. (3); see Table II]. We hesitate to claim such low activation energies for this process until further experimental studies or molecular dynamics simulations provide a better understanding of the competing atomic-scale damage and recrystallization processes. One advantage of Eq. (6) is that the experimental data can be fit quite closely, allowing for reliable extrapolation of the amorphization dose over a wide range of temperature. The critical temperature obtained from Eq. (7) is estimated to be 480 K and 620 K for the Ne^+ and the Xe^{2+} irradiations, respectively.

Attempting to determine which model is more appropriate for the current data sets is not straightforward. Physically, the difference in the two models resides in the recrystallization term. Equation (2) may be more appropriate for recombination of isolated defects in a crystalline matrix, whereas Eq. (5) models recrystallization at the amorphous-crystalline interfaces. Both processes probably occur to varying degrees, but the curve fitting suggests that the recrystallization of amorphous zones may be a more important process for the Xe^{2+} irradiations. There may be some question as to the applicability of using an amorphization-recrystallization model when the electron diffraction results in Fig. 2 suggest that amorphization occurs via an initial disordering stage. This would be true if the structure transformed uniformly and homogeneously from a defective crystal to an amorphous structure, but Eq. (6) should still be valid if the transformation is not uniform over the entire specimen. Critical temperatures and activation energies obtained from both models are given in Table II.

Ion irradiation and RBS/channeling analysis

The results of the RBS channeling measurements are summarized in Fig. 5, which also shows the RBS data for an unimplanted $Cd_2Nb_2O_7$ (111) surface for purposes of comparison. The channeling spectrum for the unimplanted samples was characterized by a minimum yield in the range of 3%–5%, and the surface peaks for Nb and Cd are clearly distinguishable. With increasing ion dose (Ne^+ or Xe^{2+}), the minimum yield from the channeling spectrum increased relatively rapidly initially and subsequently increased more slowly with increasing ion dose. Finally, at the highest doses, the RBS spectra match the random value in the near-surface region.

The effects of crystallographic orientation on the ion-damage behavior are illustrated in Fig. 6 for the case of

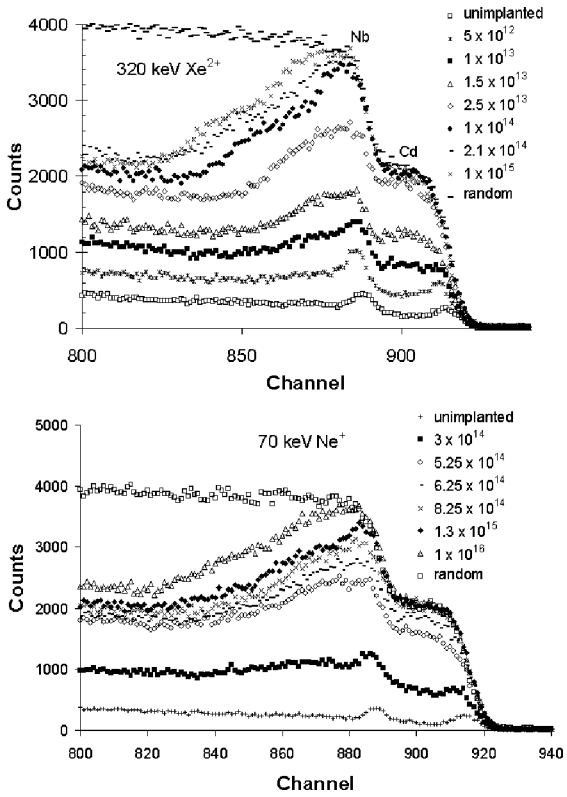

FIG. 5. Damage buildup versus ion dose as revealed by Rutherford backscattering/channeling spectra for (111) surfaces of $Cd_2Nb_2O_7$ implanted with 320-keV Xe^{2+} or 70-keV Ne^+ at the fluences indicated (in ions/cm^2). A ''rotating random'' RBS spectrum is shown for comparison.

70-keV Ne^+ irradiation of $Cd_2Nb_2O_7$. The damage level appears to increase more rapidly for irradiation along the [111] direction than along the [100] direction. The structure of cubic pyrochlore is more ''open'' along the [100] direction than along the more densely packed [111] axis. This is expected to lead to enhanced ion-channeling effects along the [100] direction, so that the energetic ions dissipate their energy while creating relatively fewer atomic displacements.[31]

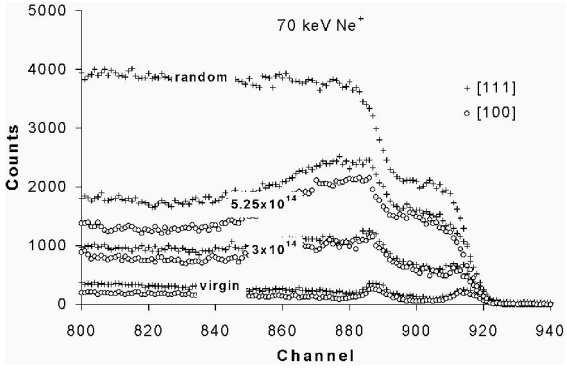

FIG. 6. Orientational dependence of the ion-damage behavior for $Cd_2Nb_2O_7$ irradiated with 70-keV Ne^+. At a dose of 5.25×10^{14} ions/cm^2 a discernable but relatively small difference is evident between the case of ions implanted along the [111] direction (crosses) and ions implanted along the [100] direction (open circles).

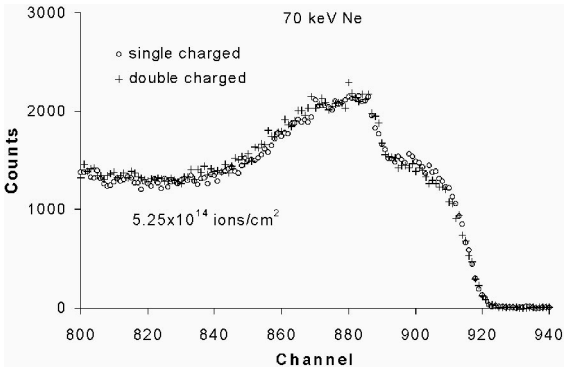

FIG. 7. Dependence of the damage buildup on the charge state of the implanted ion in $Cd_2Nb_2O_7$ implanted along the [111] direction with 70-keV Ne ions to a dose of 5.25×10^{14} ions/cm^2. Results are shown for implantation with Ne^+ (open circles) and Ne^{2+} (crosses). No dependence of the degree of radiation damage on the implanted-ion charge state is evident.

In other work, we have investigated the effects of charge conduction and dissipation during the irradiation of ABO_3 perovskite structures by changing the conductivity by many orders of magnitude using low-level doping.[32] In that case, the large difference in the electrical conductivity of the specimens was found to have no effect on the measured amorphization dose. In the present experiments, bulk single crystals of $Cd_2Nb_2O_7$ were irradiated using 70-keV Ne^+ or Ne^{2+}, i.e., singly or doubly charged ions of the same species and energy. The two RBS spectra (Fig. 7) are essentially identical after the same ion fluence, indicating that the charge state of the ion and potential charge buildup in the insulating specimen have no discernable effect on the damage accumulation in ion-irradiated pyrochlore.

In order to make valid comparisons between the ion-bombardment/RBS results and the *in situ* TEM experiments, the ion fluence for the implantation experiments should also be converted to a displacement dose using SRIM calculations. In Fig. 8(a), the depth dependences of the displacement dose, in units of dpa, for the 70-keV Ne^+ and 320-keV Xe^{2+} irradiations of bulk $Cd_2Nb_2O_7$ single crystals are shown for three different ion-implantation fluences. In Fig. 8(b), we plot the data series that most closely approximates the dose for amorphization as indicated by the raw RBS data (i.e., the data series for which the RBS/channeling yield was closest to reaching the random yield in the near surface). Also plotted in Fig. 8(b) are the dpa-vs-depth curves for the room-temperature amorphization of ion-irradiated thin foils. The amorphization dose measured in the *in situ* TEM experiments over the $\sim$100-nm specimen thickness (Table I) is about 40% less than the peak dose for amorphization measured by RBS. This apparent discrepancy will be discussed below.

The RBS/channeling data may provide an estimate of the relative amount of disorder at each implant dose. In the present case, however, interpretation of the RBS data is difficult because the Cd and Nb damage peaks overlap (see Fig. 5). In the simplest case, for disordering starting at the specimen surface, one can assume that the relative disorder (RD) is equal to $(I-I_0)/(I_r-I_0)$, where I is the measured RBS

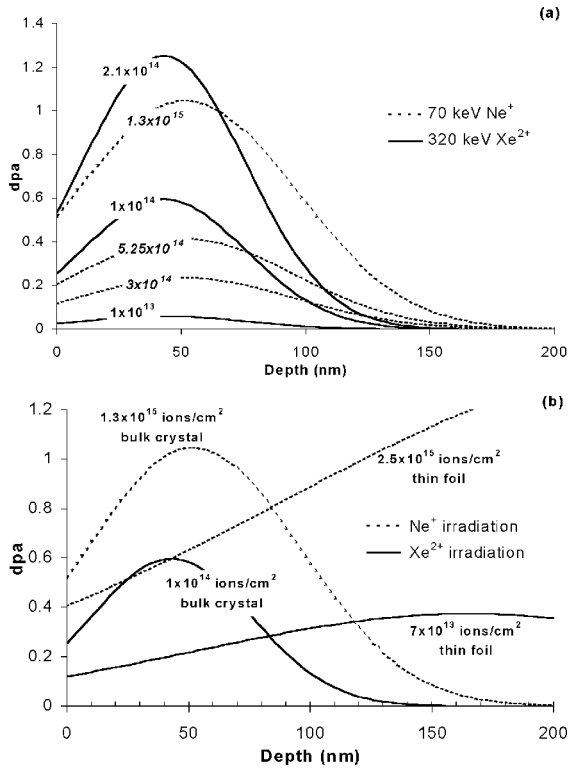

FIG. 8. (a) Depth distribution of the ion damage (in dpa) for 70-keV Ne^+ (dashed curves) and 320-keV Xe^{2+} (solid curves) irradiation of the [111] surface of $Cd_2Nb_2O_7$ single crystals. (b) Depth distributions of the ion damage for the bulk crystals and for the *in situ* TEM experiments. For the bulk-crystal RBS results, the plotted curve corresponds to the dose closest to achieving the random value in the implanted region of the bulk crystal. The damage curve for the *in situ* experiments corresponds to the fluence for amorphization, as determined by electron diffraction. Dashed curves: Ne^+ irradiation; solid curves: Xe^{2+} irradiation.

peak intensity, I_0 is the peak intensity in the unimplanted specimen, and I_r is the intensity of the random spectrum. A problem arises, however, because of the overlapping damage and surface peaks—i.e., it is not possible from the raw spectra in Fig. 5 to ascertain the depth at which the disordering begins. The damage peak for Nb overlaps the Cd damage peak; and for both Cd and Nb, the surface peak also contributes to the yield from the damaged region.

As a first approximation, we have subtracted the unimplanted spectrum from the implanted spectra in order to remove surface peak contributions (Fig. 9). The Cd peak for the intermediate damage spectra becomes resolvable at channel 900, corresponding to a backscattered He energy of 1975 keV. Using the surface energy approximation, this corresponds to a depth of 34 nm for the maximum damage peak, compared to 43 nm predicted by SRIM. In order to obtain the disordered fraction on the Cd sublattice, we simply used the ratio I/I_r obtained from Fig. 9. A more accurate analysis would take into account dechanneling effects by using a linear dechanneling approximation.[33] In the present case, because of the shallow depth of the damage peak, the short range of the incident ions, and because of the difficulty in applying the linear dechanneling approximation to these

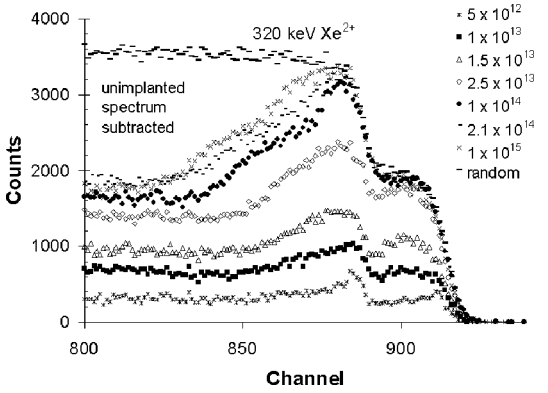

FIG. 9. RBS-channeling data for Xe^{2+}-irradiated $Cd_2Nb_2O_7$. The unimplanted spectrum was subtracted from each data series. The damage peak on the Cd sublattice is readily visible, especially at intermediate doses.

spectra (there is no way to determine where the end of the Cd damage region is actually located), we felt that the best approximation would be obtained by ignoring dechanneling effects. Using these assumptions, the disordered fraction on the Cd sublattice is plotted as a function of dose in Fig. 10.

Interpretation of the RBS yield for the Nb sublattice is more difficult. At the apparent peak of the Nb damage, there is also a contribution from He ions that are scattered from Cd at greater depth (i.e., overlapping Cd and Nb peaks). As a first approximation, one might assume that the Cd yield decreases linearly from the observed Cd peak. Because the slope of the decrease in the Cd yield cannot be accurately determined, however, the Nb data are probably too unreliable for an estimation of the disordered fraction.

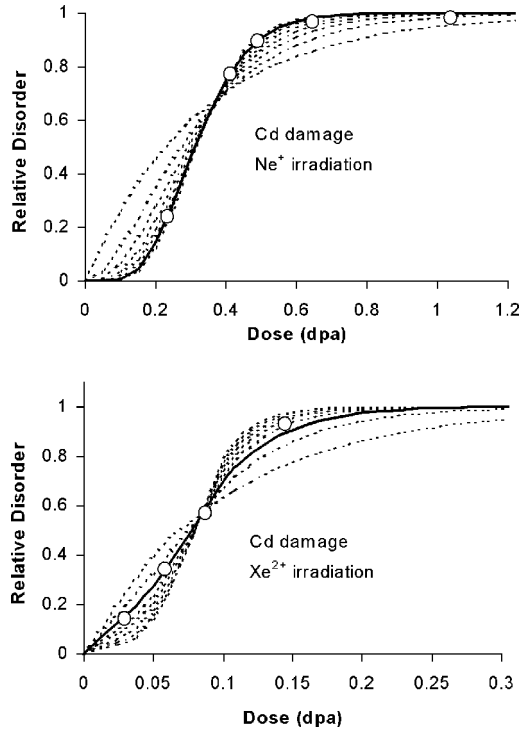

FIG. 10. Relative disorder on the Cd sublattice plotted as a function of dose for 70-keV Ne^+ (top) and 320-keV Xe^{2+} irradiation (bottom). The curves are solutions of Eq. (8) for $n=1$ to 8, and the thick solid line represents the best fit to the data.

Figure 10 shows a plot of the disordered fraction on the Cd sublattice as a function of implanted dose for both Ne^+ and Xe^{2+} irradiations. The gradual approach of the relative disorder to a value of unity (i.e., amorphization) exhibited by $Cd_2Nb_2O_7$ (as well as many other ceramic materials)[24] may account for the apparent discrepancy in the amorphization dose as measured by *in situ* TEM versus *ex situ* RBS. TEM is relatively insensitive to the presence of small quantities of crystalline material in an amorphous matrix. In fact, image simulations have shown that the best TEM can do under *ideal* conditions is to detect a level of approximately 5% of crystalline material in an amorphous matrix, although under nonideal conditions (i.e., thick specimens) considerably more crystalline material is required in order to be detected.[30] In other words, even the best sample appears amorphous above $f_a=0.95$. RBS can be sensitive to small amounts of residual crystalline order.[34] Owing to the asymptotic approach to RD=1, at high values of RD, small changes in the detectable crystalline fraction are associated with large changes in the dose (see Fig. 10). If the minimum detectable amount of residual crystallinity is only slightly lower for RBS than for TEM, this could easily account for the observed discrepancy in the amorphization dose.

The data presented in Fig. 10 can be used to evaluate the nature of the damage process. Assuming that each ion creates a cylindrical damage zone, the dose dependence of the disordered fraction can be modeled using the well-known Gibbons' equation[35]

$$\frac{A_A}{A_0}=\left[1-\left(\sum_0^n \frac{(A_iD)^{n-1}}{(n-1)!}\exp(-A_iD)\right)\right], \qquad (8)$$

where A_A is the total disordered area, A_0 is the area of the specimen, A_i is the area of a single collision cascade, A_A/A_0 is the disordered (or amorphous) fraction, D is the dose, and n is the number of cascade overlaps necessary to produce amorphization (e.g., for direct impact amorphization, $n=1$, for single overlaps $n=2$, and so on). Equation (8) has been shown by many authors to fit the f_d vs D curves. In a more recent model, Wang, Wang, and Ewing[36] have demonstrated that these curves can also be fit by assuming a direct impact amorphization model; however, the electron diffraction results in Fig. 2 are more consistent with a defect accumulation picture.

Equation (8) can be solved to fit the data plotted in Fig. 10. Using a nonlinear least-squares refinement, A_i was allowed to vary until the calculated curve best fit the experimental data. The analyses were repeated for the cases of $n=1$ (direct impact amorphization), $n=2$ (amorphization by single overlaps), and so on, until the best fit to the data was obtained, as determined from the residual of the least-squares operation. For both the Ne^+ and Xe^{2+} irradiations, the residuals of the least-squares analysis initially decreased with increasing n, reached a minimum value (i.e., the best fit), and subsequently increased.

The disorder on the Cd sublattice for the Ne^+ irradiations, along with the least-squares solutions to Eq. (8) for $n=1-8$, is shown in Fig. 10(a). In this example, the best fit to the data is provided by the $n=7$ case. In Fig. 10(b), the relative disorder on the Cd sublattice is plotted for the 320-keV Xe^{2+} irradiation of $Cd_2Nb_2O_7$. The best fit is provided by the $n=3$ ''double overlap'' case. These results suggest fundamental similarities and differences in the damage accumulation process associated with the light- and heavy-ion irradiation of $Cd_2Nb_2O_7$. For light ions, the defect density within the individual ion tracks may be so low that many cascades must strike the same area to produce the amorphous state (i.e., a defect accumulation model of amorphization). For Xe^{2+} irradiation, the data suggest that amorphization also occurs by a cascade overlap, defect accumulation process, but that fewer cascades are required.

Using the best-fit values obtained for A_i in Eq. (8), we determine a cascade area close to 1.67 nm^2 for the Ne^+ irradiation of $Cd_2Nb_2O_7$. For the Xe^{2+} irradiations, the best fit of Eq. (8) gave $A_i=20.75$ nm^2. The estimated cascade area is, therefore, 12.4 times larger for the Xe^{2+} irradiation than for Ne^+. Additionally, the model suggests that $\sim$ three ion impacts are required for amorphization with 320-keV Xe^{2+}, whereas, as many as seven may be necessary for the 70-keV Ne^+ irradiation. Since each Xe cascade is larger by a factor of 12.4 and, according to the model, only $\sim 3/7$ of the number of ion impacts are required, then the Xe ion fluence for amorphization should be lower by a factor of $12.4\times 7/3=29$. The actual difference in the ion fluence for amorphization of $Cd_2Nb_2O_7$ at room temperature measured in the *in situ* TEM experiments is lower by a factor of 36 for the Xe^{2+} irradiations compared to Ne^+ (Table I). Considering the numerous assumptions implicit in the model and in the interpretation of the RBS data, this difference of only 20% is evidence supporting the above analysis.

Comparison with previous data

In all previous *in situ* irradiation studies of pyrochlore,[15–17] a disordering of the *A*- and *B*-site cations was reported at low to intermediate ion doses (~ 0.3–0.5 D_c), as observed here for $Cd_2Nb_2O_7$. Wang *et al.*[17] reported that amorphization and cation disordering occur concurrently in titanate pyrochlores; however, our results in Fig. 2 are consistent with the near completion of disordering *prior* to the onset of amorphization. The critical temperature for Xe^{2+} irradiation estimated from Eq. (7) (620 K) is lower than the values reported for Xe-ion irradiation of titanate pyrochlores (Table III). In contrast, the room-temperature amorphization dose reported here for $Cd_2Nb_2O_7$ (0.22 dpa) is considerably less than that required to amorphize Gd- and rare-earth-titanate pyrochlores (0.50 to 0.80 dpa).[16,17] These large differences cannot be attributed to the different Xe-ion energies, since the doses are normalized in dpa units.

The results show that $Cd_2Nb_2O_7$ is more susceptible to irradiation-induced amorphization below room temperature than the titanate pyrochlores, but that recovery is more efficient at high temperatures. For many materials there is an inverse correlation of T_c with D_c (room temperature), particularly within groups of phases having the same crystal structure [e.g., Refs. 29 and 37]. In other words, the T vs D_c curves (i.e., Fig. 4) generally do not cross. This is true for Xe irradiation of pyrochlores with A,B cation valences of $+3,+4$, but the $+2,+5$ compound $Cd_2Nb_2O_7$ does not fit the general trend. Sickafus *et al.*[3] suggested that irradiation-induced amorphization in $+3,+4$ pyrochlores is controlled by cation radius ratios through their influence on antisite defect formation energies. According to this model, phases that have radius ratios close to 1:1 have low antisite defect energies and can accommodate radiation damage by cation disordering, without amorphization. $Cd_2Nb_2O_7$ has an A:B cation radius ratio of 1.72:1 (radii from Ref. 38), similar to that of $Gd_2Ti_2O_7$ (1.74:1). Accordingly, these phases might be expected to demonstrate a similar resistance to amorphization. Taking either T_c or room temperature D_c (Table III) as a measure of the radiation resistance shows that $Gd_2Ti_2O_7$ and $Cd_2Nb_2O_7$ are, in fact, quite different. If the defect energy picture of amorphization is valid, the relationship between the radius ratios and the antisite defect energies in the $+2,+5$ pyrochlores must be very different from the $+3,+4$ phases. Determination of physical reason for the difference between $Cd_2Nb_2O_7$ and the $+3,+4$ pyrochlores will require further systematic studies on additional $+2,+5$ phases.

TABLE III. Summary *in situ* ion irradiation data for the oxide pyrochlores.

Phase	Ion	D_c (dpa) [a]	T_c (K)
$Gd_2Ti_2O_7$ [b]	1.5 MeV Xe	0.63	1030
$Gd_2Ti_2O_7$ [b]	1.0 MeV Kr	0.50	840
$Gd_2Ti_2O_7$ [b]	0.6 MeV Ar	0.60	680
$(Gd_{0.95}Ca_{0.05})_2Ti_2O_7$ [c]	1.0 MeV Kr	n.a. [g]	1010
$Y_2Ti_2O_7$ [c]	1.0 MeV Xe	0.80	780
$Eu_2Ti_2O_7$ [c]	1.0 MeV Kr	n.a.	1080
$Sm_2Ti_2O_7$ [c]	1.0 Me Kr	n.a.	1060
$Er_2Zr_2O_7$ [d]	0.35 MeV Xe		
$Gd_2Zr_2O_7$ [e]	1.0 MeV Kr		
$Cd_2Nb_2O_7$ [f]	1.2 MeV Xe	0.22	620
$Cd_2Nb_2O_7$ [f]	0.28 MeV Ne	0.65	480

[a]At room temperature.
[b]From Ref. 16.
[c]From Ref. 17.
[d]From Ref. 3.
[e]From Ref. 10.
[f]This work.
[g]n.a. indicates that the authors did not provide an amorphization dose.

SUMMARY AND CONCLUSIONS

The pyrochlore composition $Cd_2Nb_2O_7$ can be readily amorphized by either Ne^+ or Xe^{2+} irradiation. For the case of Ne^+ ion irradiations, the amorphization dose is three times higher at low temperatures than for Xe^{2+}, and the critical temperature is lower by approximately 140 K. The

amorphization dose, as measured by RBS, was approximately 40% higher than that measured by *in situ* irradiation in the TEM, possibly due to the greater sensitivity of RBS to the presence of residual crystalline regions. The damage accumulation was only weakly dependent on the crystallographic orientation of the specimen. No measurable dependence of damage accumulation on the ion charge state (1+ vs 2+) was observed. A simple amorphization-recrystallization model was developed and compared to a previous model. Both the electron diffraction results and the dose dependence of the damage accumulation suggest that amorphization occurs by a multi-cascade-overlap, defect-accumulation process for irradiation with both types of ion. $Cd_2Nb_2O_7$ has a lower amorphization dose at room temperature and a lower critical temperature than the titanate pyrochlores, suggesting that the antisite defect-energy picture proposed to explain the relative radiation resistance of the +3,+4 cation valence pyrochlores cannot be straightforwardly extended to +2,+5 pyrochlores.

ACKNOWLEDGMENTS

We thank the staff at the HVEM-Tandem Facility at Argonne National Laboratory for assistance with the ion irradiations. Bill Weber and Ray Zuhr provided careful reviews, especially concerning interpretation of the RBS data, which considerably improved this manuscript. Jie Lian provided the crystal structure diagram. A.M. acknowledges support from the Natural Sciences and Engineering Research Council of Canada. L.A.B. was supported by the U.S. Department of Energy, Division of Materials Sciences and the Environmental Management Sciences Program, and R.C.E. by Basic Energy Sciences/USDOE Grant No. DE-FG02-97ER45656. The assistance of Ed Sonder with the ion implantation experiments and of Joanne Ramey with the crystal growth is gratefully acknowledged. Oak Ridge National Laboratory is managed by the U.S. Department of Energy under Contract No. DE-AC05-00OR22725, managed by UT-Battelle, LLC.

*Present address: National Center for Physical Acoustics, The University of Mississippi, University, MS 38677.

[1] A. E. Ringwood, S. E. Kesson, K. D. Reeve, D. M. Levins, and E. J. Ramm, in Radioactive Waste Forms for the Future, edited by W. Lutze and R. C. Ewing (North-Holland, Amsterdam, 1988), pp. 233–334.

[2] A. Jostsons, L. Vance, and B. Ebbinghaus, *Immobilization of Surplus Plutonium in Titanate Ceramics*, Proceedings of the International Conference on Future Nuclear Systems, Global 99, Jackson Hole, Wyoming (American Nuclear Society CDROM, 1999).

[3] K. E. Sickafus, L. Minervini, R. W. Grimes, J. A. Valdez, M. Ishimaru, F. Li, K. J. McClellan, and T. Hartmann, Science **289**, 748 (2000).

[4] H. von Gaertner, Neues Jahrb. Mineral., Geol. Palaeontol., Monatsh., Abt. 1 **61**, 1 (1930).

[5] R. A. McCauley, J. Appl. Phys. **51**, 290 (1980).

[6] E. Aleshin and R. Roy, J. Am. Ceram. Soc. **45**, 18 (1962).

[7] B. C. Chakoumakos and R. C. Ewing, in *Scientific Basis for Nuclear Waste Management VIII*, edited by C. M. Jantzen, J. A. Stone, and R. C. Ewing, MRS Symposia Proceedings No. 439 (Materials Research Society, Pittsburgh, PA, 1997), pp. 641–646.

[8] E. R. Vance, M. W. A. Stewart, and G. R. Lumpkin, J. Mater. Sci. **26**, 2694 (1991).

[9] S. S. Shoup, C. E. Bamberger, and R. G. Haire, J. Am. Ceram. Soc. **79**, 1489 (1996).

[10] S. X. Wang, B. D. Begg, L. M. Wang, R. C. Ewing, W. J. Weber, and K. V. G. Kutty, J. Mater. Res. **14**, 4470 (1999).

[11] F. W. Clinard, Jr., D. E. Peterson, D. L. Rohr, and L. W. Hobbs, J. Nucl. Mater. **126**, 245 (1989).

[12] P. E. Raison, R. G. Haire, T. Sato, and T. Ogawa, in *Scientific Basis for Nuclear Waste Management XXI*, edited by D. J. Wronkiewicz and J. H. Lee, MRS Symposia Proceedings No. 556 (Materials Research Society, Pittsburgh, PA, 1999), pp. 3–9.

[13] W. J. Weber, J. W. Wald, and Hz. Matzke, Mater. Lett. **3**, 173 (1985).

[14] G. R. Lumpkin and R. C. Ewing, Phys. Chem. Miner. **16**, 2 (1988).

[15] K. L. Smith, N. J. Zaluzec, and G. R. Lumpkin, J. Nucl. Mater. **250**, 36 (1997).

[16] S. X. Wang, L. M. Wang, R. C. Ewing, G. S. Was, and G. R. Lumpkin, Nucl. Instrum. Methods Phys. Res. B **149**, 704 (1999).

[17] S. X. Wang, L. M. Wang, R. C. Ewing, and K. V. G. Kutty, Nucl. Instrum. Methods Phys. Res. B **169**, 135 (2000).

[18] C. W. Allen and E. A. Ryan, in *Microstructure Evolution During Irradiation*, edited by I. M. Robertson, G. S. Was, L. W. Hobbs, and T. Diaz de la Rubia, MRS Symposia Proceedings No. 439 (Materials Research Society, Pittsburgh, PA, 1997), pp. 277–288.

[19] J. F. Ziegler, *SRIM* (IBM Research, Yorktown, NY, 1999).

[20] K. A. Jackson, J. Mater. Res. **3**, 1218 (1988).

[21] G. Carter and M. J. Nobes, J. Mater. Res. **6**, 2103 (1991).

[22] V. Heera, T. Henkel, R. Kögler, and W. Skorupa, Phys. Rev. B **52**, 15 776 (1995).

[23] S. X. Wang, L. M. Wang, R. C. Ewing, and R. H. Doremus, J. Non-Cryst. Solids **238**, 198 (1998).

[24] W. J. Weber, Nucl. Instrum. Methods **166**, 98 (2000).

[25] A. Meldrum, L. A. Boatner, S. J. Zinkle, and R. C. Ewing, Phys. Rev. B **59**, 3981 (1999).

[26] W. J. Weber, R. C. Ewing, and L. M. Wang, J. Mater. Res. **9**, 688 (1994).

[27] A. Meldrum, L. A. Boatner, W. J. Weber, and R. C. Ewing, Geochim. Cosmochim. Acta **62**, 2509 (1998).

[28] S. X. Wang, G. R. Lumpkin, L. M. Wang, and R. C. Ewing, Nucl. Instrum. Methods Phys. Res. B **166-167**, 293 (2000).

[29] A. Meldrum, L. A. Boatner, L. M. Wang, and R. C. Ewing, Phys. Rev. B **56**, 13 805 (1997).

[30] M. L. Miller and R. C. Ewing, Ultramicroscopy **48**, 203 (1992).

[31] M. T. Robinson, J. Nucl. Mater. **216**, 1 (1994).

[32] A. Meldrum (unpublished).

[33] O. W. Holland, D. Fathy, J. Narayan, and O. S. Oen, Radiat. Eff. **90**, 127 (1985).

[34] W.-K. Chu, J. W. Mayer, and M.-A. Nicolet, *Backscattering Spectrometry* (Academic Press, New York, 1978).
[35] J. F. Gibbons, Proc. IEEE **60**, 1062 (1972).
[36] S. X. Wang, L. M. Wang, and R. C. Ewing, Phys. Rev. B (to be published).
[37] L. M. Wang, S. X. Wang, W. L. Gong, and R. C. Ewing, Nucl. Instrum. Methods Phys. Res. B **141**, 501 (1998).
[38] R. D. Shannon, Acta Crystallogr., Sect. A: Cryst. Phys., Diffr., Theor. Gen. Crystallogr. **32**, 751 (1976).